ALMA MATER STUDIORUM
UNIVERSITÀ DI BOLOGNA

DEPARTMENT OF ELECTRICAL, ELECTRONIC, AND INFORMATION ENGINEERING “GUGLIELMO MARCONI” – DEI

SECOND CYCLE DEGREE IN BIOMEDICAL ENGINEERING
INNOVATIVE TECHNOLOGIES IN DIAGNOSTICS AND THERAPY
Class: LM-21

Computational Modeling of Isolated Cardiomyocytes in Heart Failure with Reduced Ejection Fraction

Dissertation in
Computational Cardiology

Supervisor
Prof. Stefano Severi

Defended by
Sama Valipourmakouei

Co-Supervisor
Prof. Eugenio Ricci

Academic Year 2025/2026
Graduation Session V

To my father, who saw the seed of my journey planted and now watches its completion from the sky.

Contents

List of Figures

List of Tables

Abbreviations

Abbreviation	Meaning
AP	Action potential
APD	Action potential duration
APD_{50}	Action potential duration at 50% repolarization
APD_{90}	Action potential duration at 90% repolarization
ATP	Adenosine triphosphate
AT	Active tension
ATpeak	Peak active tension
ATmin	Minimum active tension
BCL	Basic cycle length
BPSLand	Human ventricular electromechanical cardiomyocyte model (BPS2020 + Land-type contraction; Bartolucci et al., 2022)
BPS2020	Human ventricular electrophysiology and Ca^{2+}-handling model (Bartolucci–Passini–Severi, 2020)
CaT	Intracellular calcium transient
CaDiast	Diastolic intracellular calcium level
CaSyst	Systolic intracellular calcium level
$CaTD_{50}$	Calcium transient duration to 50% decay
$CaTD_{90}$	Calcium transient duration to 90% decay
CaMKII	Ca^{2+}/calmodulin-dependent protein kinase II
CaMKa	CaMKII activity (model variable)
cAMP	Cyclic adenosine monophosphate
CDI	Calcium-dependent inactivation
CICR	Calcium-induced calcium release
CTRL	Control condition
CV	Conduction velocity

Abbreviation	**Meaning**
DAD	Delayed afterdepolarization
DevF	Developed force ($\mathrm{AT_{peak}} - \mathrm{AT_{min}}$)
$\mathrm{dV/dt_{max}}$	Maximum action-potential upstroke velocity (mV/ms)
EAD	Early afterdepolarization
EC coupling	Excitation–contraction coupling
HF	Heart failure
HFrEF	Heart failure with reduced ejection fraction
HFpEF	Heart failure with preserved ejection fraction
I_{CaL}	L-type calcium current
I_{K1}	Inward rectifier potassium current
I_{Kr}	Rapid delayed rectifier potassium current
I_{Ks}	Slow delayed rectifier potassium current
I_{NaK}	$\mathrm{Na^+/K^+}$ ATPase pump current
I_{NaL}	Late sodium current
I_{to}	Transient outward potassium current
Jrel	SR $\mathrm{Ca^{2+}}$ release flux
Jup	SR $\mathrm{Ca^{2+}}$ uptake flux
Jleak	SR $\mathrm{Ca^{2+}}$ leak flux
NCX	$\mathrm{Na^+/Ca^{2+}}$ exchanger
ODE	Ordinary differential equation
ORd	O'Hara–Rudy ventricular model
RyR	Ryanodine receptor
SERCA	Sarco/endoplasmic reticulum $\mathrm{Ca^{2+}}$-ATPase
SR	Sarcoplasmic reticulum
ToR-ORd	Tomek–O'Hara–Rudy model
TTP	Time to peak
RT50	Relaxation time to 50% of peak tension
RMP	Resting membrane potential
n_b	Number of paced beats
Vpeak	Peak membrane voltage
Vm	Transmembrane voltage

Abstract

This thesis adopts the BPSLand human ventricular cardiomyocyte model to investigate how heart failure with reduced ejection fraction (HFrEF) remodeling alters coupled electrophysiology, intracellular Ca^{2+} handling, and contractile function in a controlled *in silico* setting. Control and HFrEF conditions were simulated under a fixed pacing protocol until steady state, and membrane voltage, Ca^{2+} transient, L-type Ca^{2+} current, and active tension signals were analyzed using a consistent biomarker-based workflow. Remodeling effects were quantified through HF/CTRL ratios and relative changes and compared with trends reported by state-of-the-art human ventricular computational studies and, where available, with experimental ranges.

The simulations reproduced key HFrEF signatures, including prolonged repolarization and altered Ca^{2+} cycling, and revealed waveform-level links between plateau dynamics, Ca^{2+} entry, and downstream Ca^{2+} handling. Agreement with published reference trends was stronger for electrical and Ca^{2+}-related biomarkers than for tension kinetics, highlighting the higher sensitivity of mechanical outputs to electromechanical coupling assumptions and biomarker definitions. A robustness assessment confirmed stable biomarker ratios within the tested steady-state pacing settings.

Overall, the work establishes BPSLand as a platform to quantify cross-domain HFrEF remodeling and provides a baseline for future model refinement and *in silico* evaluation of candidate therapeutic strategies targeting electrophysiology and Ca^{2+} handling.

Chapter 1

Introduction

1.1 Problem statement and approach

Heart failure (HF) is a progressive syndrome in which the heart cannot provide adequate perfusion to meet metabolic demands, and it remains a major contributor to morbidity and mortality worldwide. This thesis focuses on heart failure with reduced ejection fraction (HFrEF), where impaired systolic function is accompanied by coupled remodeling of electrophysiology, intracellular Ca^{2+} handling, and contractile performance at the cardiomyocyte level.

At the cellular level, HFrEF frequently exhibits delayed repolarization and prolonged action potential duration (APD), reflecting a reduced repolarization reserve due to coordinated changes in inward and outward membrane currents. Because action potential morphology modulates Ca^{2+} entry through I_{CaL} and thereby influences intracellular Ca^{2+} loading, electrical remodeling can propagate into Ca^{2+} cycling and contraction. In parallel, excitation–contraction coupling dysfunction (e.g., depressed SR Ca^{2+} uptake, altered release, and impaired microdomain coupling) can reduce systolic Ca^{2+} release, slow Ca^{2+} removal, diminish twitch force, and delay relaxation. Beyond reduced peak force, HFrEF is also characterized by impaired contractile reserve, commonly reflected by a blunted or negative force–frequency relationship, which integrates changes in Ca^{2+} influx, SR uptake, extrusion, and buffering.

Despite major experimental advances, human cardiomyocyte characterization in HF remains limited by constrained tissue access, protocol variability, and the difficulty of simultaneously resolving voltage, Ca^{2+}, and force with comparable temporal precision. Computational electromechanical modeling addresses this gap by providing a controlled environment where specific remodeling components can be isolated and evaluated systematically. By coupling detailed human ventricular ionic/Ca^{2+} models to biophysically-based myofilament formulations, electromechanical frameworks enable simulation of the full excitation–contraction cycle and support mechanistic interpretation of how remodeling shapes AP and Ca^{2+} transients and their mechanical consequences under fixed pacing conditions.

In this thesis, these questions are investigated using the BPSLand human ventricular electromechanical model as the primary simulation platform. A literature-derived remodeling map (Mora et al.) is used as an external reference to define remodeling targets and expected qualitative trends. Model outputs are then summarized through a consistent set of electrophysiological, Ca^{2+}-handling, and contraction biomarkers extracted from membrane voltage, intracellular Ca^{2+}, I_{CaL}, and active tension.

1.2 Physiological background

This work models an *isolated human ventricular cardiomyocyte* paced by an external stimulus current at a prescribed basic cycle length (BCL). The simulated outputs analyzed throughout the thesis are the transmembrane action potential (AP), the intracellular Ca^{2+} transient (CaT), the L-type Ca^{2+} current I_{CaL}, and the resulting *isometric active tension.* Within this single-cell electromechanical framework, AP morphology (e.g., APD_{50} and APD_{90}) influences Ca^{2+} entry via I_{CaL}, which triggers SR Ca^{2+} release and shapes CaT amplitude and decay; CaT then regulates myofilament activation and twitch tension. Tissue-level propagation, chamber geometry, and ECG signals are outside the scope of this study and are not modeled explicitly.

1.2.1 Pacing protocol

In the intact heart, ventricular excitation is initiated by the specialized conduction system (SA node, AV node, His–Purkinje network), which ensures rapid and coordinated activation of the ventricles [33]. In a single-cell model, these spatial propagation mechanisms are not represented. Instead, activation is reproduced by injecting a brief stimulus current, and rate is controlled via the BCL. This pacing abstraction enables systematic study of rate-dependent changes in AP, CaT, and tension under controlled conditions, without confounding effects from propagation, heterogeneity, or electrotonic coupling.

1.2.2 Ventricular action potential

The ventricular action potential (AP) is the time course of transmembrane voltage during one excitation–contraction cycle. It reflects the coordinated gating of ion channels controlling Na^{+}, Ca^{2+}, and K^{+} fluxes across the sarcolemma. At rest, ventricular cells maintain a membrane potential of approximately -80 to -90 mV, primarily determined by high K^+ permeability and the inward rectifier current I_{K1} [33].

Upon stimulation, channels activate in a stereotyped sequence that produces the characteristic ventricular AP with a prominent plateau phase. Figure 1.1 illustrates the conventional subdivision into phases 0–4 [33, 7].

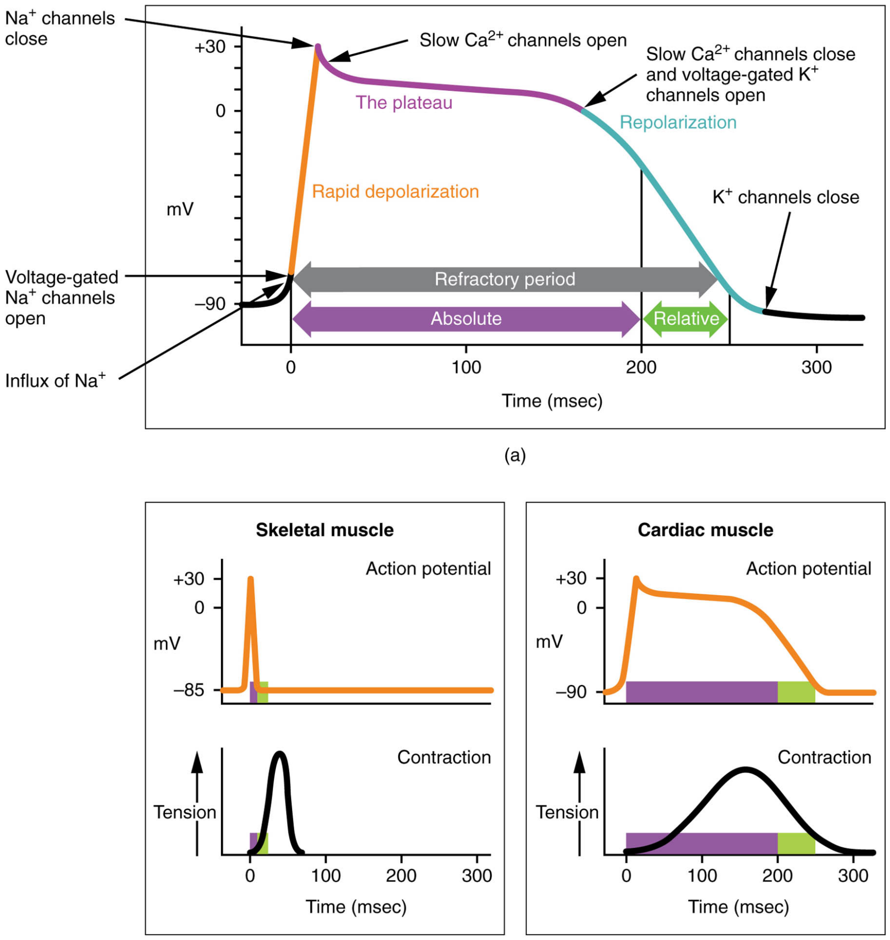

(a)

(b)

Figure 1.1: Schematic ventricular action potential with phases 0–4 [33].

- **Phase 0 – Rapid depolarization.** Activation of fast Na^+ channels generates the upstroke via I_{Na}, rapidly driving the membrane toward positive potentials and initiating excitation.

- **Phase 1 – Early repolarization.** Na^+ channel inactivation and activation of the transient outward K^+ current I_{to} produce a brief partial repolarization.

- **Phase 2 – Plateau phase.** A near-balance between inward L-type Ca^{2+} current I_{CaL} and outward K^+ currents sustains the plateau. Ca^{2+} entry through I_{CaL} is the key trigger for SR Ca^{2+} release, thereby linking electrical activity to CaT generation and downstream contraction.

- **Phase 3 – Repolarization.** Inactivation of I_{CaL} and increasing activity of delayed rectifier K^+ currents (I_{Kr}, I_{Ks}), together with I_{K1} late in repolarization, restore the membrane potential toward rest.

- **Phase 4 – Resting state.** Resting potential is maintained mainly by I_{K1} and by ionic pumps and exchangers, including the Na^+/K^+ ATPase, which preserve transmembrane gradients between beats.

AP morphology is a central determinant of Ca^{2+} entry and intracellular loading: changes in plateau level and duration directly influence the time integral of I_{CaL} and thus the trigger for SR Ca^{2+} release [23]. Accordingly, AP duration biomarkers (APD_{50} and APD_{90}) provide compact descriptors of repolarization changes that are mechanistically coupled to CaT morphology and, ultimately, twitch tension [23]. In HFrEF, reduced repolarization reserve commonly leads to APD prolongation, making APD-based metrics a primary readout for CTRL vs. HF comparisons [22].

1.3 HFrEF at the Cardiomyocyte Level

At the single-cell scale, HFrEF is characterized by coupled remodeling of electrophysiology, Ca^{2+} handling, and contraction. Repolarization is often prolonged due to reduced repolarization reserve, leading to increased APD and altered plateau dynamics. In parallel, Ca^{2+} cycling is impaired, typically with a smaller Ca^{2+} transient and slower Ca^{2+} removal driven by an imbalance between SR uptake/release and sarcolemmal extrusion. These changes translate into reduced twitch tension, slower force development, and delayed relaxation. Structural remodeling, including partial detubulation and dyadic disruption, further reduces EC-coupling gain by weakening local LTCC–RyR coupling and promoting spatially dyssynchronous Ca^{2+} release [22, 20, 21, 25, 26]. These mechanisms motivate the remodeling targets summarized in Mora *et al.* and implemented in the present modeling framework [3].

1.3.1 Electrophysiological remodeling

A common electrophysiological signature of HFrEF is APD prolongation, reflecting reduced repolarization reserve due to coordinated changes in inward and outward currents [22, 29]. This alters late repolarization dynamics and can increase sensitivity of AP duration to perturbations [30]. Because AP morphology modulates I_{CaL} and thus Ca^{2+} entry, electrical remodeling propagates into Ca^{2+} cycling and contraction [23]. In this work, APD_{50} and APD_{90} are used as primary indicators of repolarization changes.

1.3.2 Ca^{2+} handling

HFrEF Ca^{2+} dysregulation typically presents as reduced CaT amplitude and slower decay, consistent with depressed SERCA-mediated reuptake, enhanced NCX-mediated extrusion, and altered RyR function (e.g., increased diastolic leak or modified release sensitivity) [20, 27]. These changes reduce SR Ca^{2+} content and effective systolic release while slowing cytosolic Ca^{2+} removal, thereby impairing force development and relaxation. Ca^{2+} handling also feeds back to voltage through electrogenic transport (notably NCX), contributing to coupled EP–Ca^{2+} effects [28]. The CaT biomarkers reported later quantify both magnitude and kinetics of this dysfunction.

1.3.3 T-tubules and dyads

Microstructural remodeling in HFrEF includes disruption and loss of the transverse (t)-tubule network (*partial detubulation*), which weakens dyadic coupling between LTCC and RyR clusters [25, 26]. The resulting increase in “orphaned” RyR sites promotes spatially dyssynchronous Ca^{2+} release and reduces EC-coupling gain, reshaping CaT morphology and its translation into force [3]. In the Mora/ToR-ORd framework, these effects are represented by redistributing dyadic vs. non-dyadic LTCC and NCX contributions and increasing the fraction of orphaned RyRs [3].

1.4 Modeling Framework and Reference Models

The modeling strategy combines (i) a *reference remodeling map* used to define literature-supported HFrEF targets and the expected qualitative direction of biomarker changes, and (ii) a *primary electromechanical simulation platform* used to implement remodeling and quantify its consequences. Specifically, the HFrEF remodeling framework by Mora et al. (based on a ToR-ORd+Land electromechanical formulation) is used as an external benchmark for remodeling directionality and plausibility, whereas all simulations and biomarker quantification in this thesis are performed with the BPSLand human ventricular electromechanical model as the primary platform [3, 6]. The electrophysiology-only BPS2020 study is referenced to document the revised Ca^{2+} handling and I_{CaL} formulation inherited by BPSLand [5, 6].

Across baseline and remodeled conditions, biomarkers are extracted in a standardized manner spanning: (i) AP morphology and repolarization (APD_{50}, APD_{90}, V_{peak}, RMP, dV/dt_{max}), (ii) Ca^{2+}-transient magnitude and kinetics (CaDiast, CaSyst, $CaTD_{50}$, $CaTD_{90}$), and (iii) active-tension magnitude and timing (ATpeak, ATmin, DevF, TTP, RT50), consistent with the biomarker definitions and validation workflow reported for BPSLand [6].

1.4.1 Reference framework: Mora/ToR-ORd

The remodeling framework proposed by Mora et al. is used in this thesis as a *reference* to define literature-supported HFrEF targets and to establish expected qualitative trends and plausible ranges for key biomarkers in failing human ventricular myocytes [3]. Here, “ranges” refer to the HF/CTRL ratios reported by Mora et al., which compile both model-derived ratios (ToR-ORd electromechanical simulations) and experimental HF/CTRL ranges from the cited literature. Importantly, Mora et al. is not used as the simulation engine in this thesis; instead, it serves as an external benchmark to interpret whether the phenotype implemented in BPSLand reproduces coherent cross-domain trends (AP, Ca^{2+} transient, and tension) under HFrEF-like perturbations.

ToR-ORd electromechanical baseline

Mora et al. built their reference framework on the ToR-ORd model, a calibrated refinement within the O’Hara–Rudy (ORd) family of human ventricular models [8]. ORd-lineage models provide detailed formulations of transmembrane ionic currents and intracellular Ca^{2+} cycling, supporting robust simulation of ventricular AP morphology, rate dependence, and Ca^{2+} dynamics [7]. The ToR-ORd electrophysiology–Ca^{2+} model has been coupled to a Land-type myofilament formulation by the Oxford group to form an electromechanical human ventricular cardiomyocyte model [48]. Mora et al. then used this electromechanical framework to investigate HFrEF remodeling and to report expected HF/CTRL trends across AP, Ca^{2+} transients, and force biomarkers [3].

Table 1.1: Main HFrEF remodeling scalings reported by Mora et al. (HF relative to CTRL; ToR-ORd baseline) [3].

Target (Mora et al.)	**HF scaling (×CTRL)**
I_{NaL}	1.30
τ_{hL}	1.80
I_{to}	0.40
I_{K1}	0.68
I_{NaK}	0.70
NCX	1.65
CaMKII activity	1.50
SERCA	0.45
J_{leak}	1.30
$K_{\mathrm{rel,Ca}}$	0.80

Remodeling targets and expected trends

Table 1.1 reports the main HFrEF remodeling scalings adopted by Mora et al. with respect to the ToR-ORd baseline (Supplementary Table S1) [3]. The reported factors represent relative changes in key ionic and Ca^{2+}-handling targets (e.g., maximal current/flux amplitudes and selected kinetics), and are used in this thesis as an external reference to (i) define the expected direction of HF/CTRL biomarker changes and (ii) check cross-domain consistency across action potential, Ca^{2+} transient, and mechanical outputs. Structural (t-tubule/dyadic) and myofilament components included in Mora et al. are described separately in the original work and are not fully summarized by the ionic scaling factors alone [3].

1.4.2 BPSLand electromechanical model

All simulations in this thesis were performed using *BPSLand*, a validated adult human ventricular electromechanical cardiomyocyte model that integrates BPS2020 electrophysiology/Ca^{2+} handling with the Land contractile element (LandCE) to generate isometric active tension [6, 9]. BPS2020 belongs to the O'Hara–Rudy (ORd) lineage and includes an updated I_{CaL} formulation and Ca^{2+}-handling refinements to reproduce key human behaviors, including the inverse dependence of action potential duration on extracellular Ca^{2+} [5, 6].

Electrophysiology and Ca^{2+} cycling (BPS2020). At a functional level, the EP and Ca^{2+} subsystems provide the excitation–contraction "front end": membrane

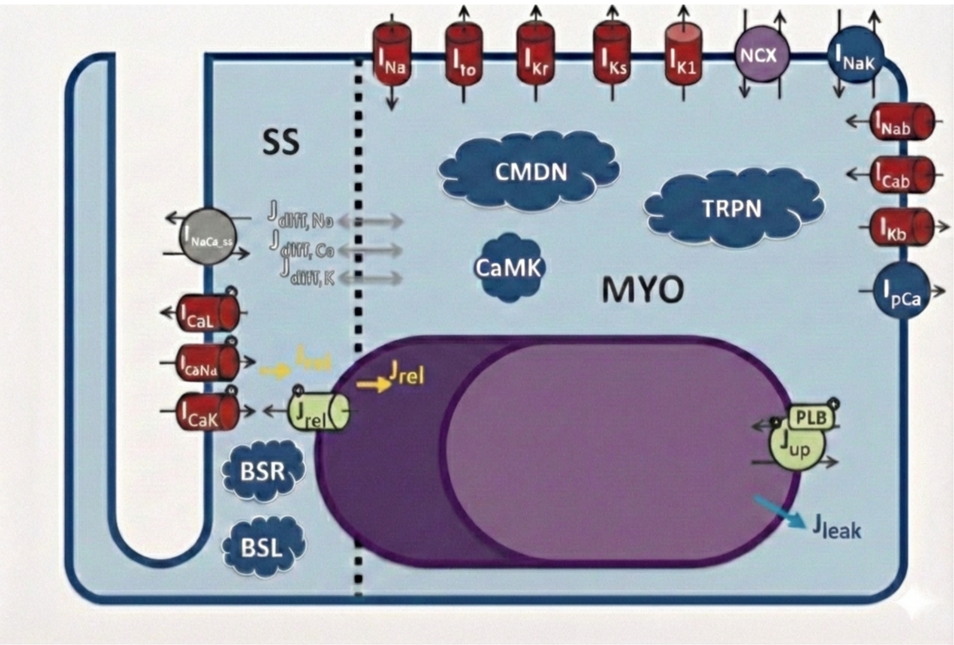

Figure 1.2: BPS2020 electrophysiology and Ca^{2+}-handling schematic (Land contractile element excluded), showing the main compartments (subspace, bulk myoplasm, SR) and principal fluxes controlling Ca^{2+} cycling (release J_{rel}, uptake J_{up}, and leak J_{leak}), together with representative sarcolemmal currents and transporters. Adapted from the BPSLand/BPS2020 model description [6].

currents shape the action potential (AP), and Ca^{2+} fluxes shape the intracellular Ca^{2+} transient (CaT) that activates contraction. In BPS2020, cytosolic Ca^{2+} is represented using two domains (subspace and bulk myoplasm), while the SR Ca^{2+} dynamics are summarized by release, uptake, and leak fluxes (J_{rel}, J_{up}, J_{leak}) [6]. The sarcolemma includes the main depolarizing and repolarizing currents (e.g. Na^{+}, Ca^{2+}, and K^{+} currents), together with electrogenic transporters and pumps (e.g. NCX and I_{NaK}) [6]. Figure 1.2 summarizes the compartmental organization and the dominant Ca^{2+} pathways used in this work. For clarity, this schematic is intended as a *representative* overview of the major mechanisms rather than an exhaustive inventory of every current and sub-component.

Contractile element and coupling (LandCE). Mechanical activity in BPS-Land is provided by LandCE, which converts the cytosolic Ca^{2+} signal into isometric active tension through thin-filament regulation and cross-bridge cycling [9, 6]. A key feature is *bidirectional* coupling: Ca^{2+} binding to troponin in the myofilament module contributes to the overall Ca^{2+} buffering balance, so changes in contractile-state occupancy can feed back onto the free CaT [6]. Figure 1.3

shows the LandCE state structure used to represent thin-filament regulation and cross-bridge kinetics.

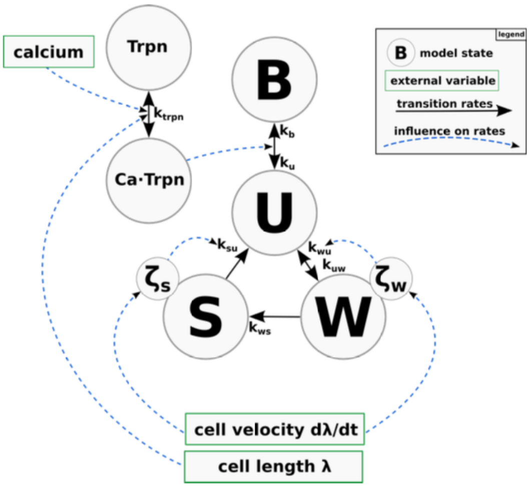

Figure 1.3: Land contractile element (LandCE) state diagram: Ca^{2+}*-troponin binding regulates thin-filament activation and transitions among cross-bridge states. Rate constants depend on Ca*$^{2+}$ *and kinematic variables (*λ*,* $d\lambda/dt$*). Adapted from [9].*

The simulated waveforms (AP, CaT, I_{CaL}, and active tension) provide the signals used for biomarker extraction as defined in Methods.

1.4.3 Scope and modeling assumptions

The simulations in this thesis are intentionally confined to the *isolated single-cell* level. This choice enables controlled, mechanistic attribution of remodeling effects, but it also defines what the framework does *not* represent. Moreover, the literature data used to parameterize and validate the remodeling scenarios considered here are predominantly available at the single-cell level, which further motivates this modeling scope.

Electrical scope. The model describes a single ventricular cardiomyocyte under a fixed pacing protocol. It does not represent tissue-level propagation, cell-to-cell coupling, or spatial heterogeneity across the ventricular wall beyond selecting a single-cell parameter set; consequently, ECG-level signals and conduction-related phenomena are not generated directly.

Mechanical scope. Mechanical outputs should be interpreted as *cell-level isometric active tension* generated by the embedded myofilament model (LandCE), not as chamber pressure–volume behavior. The mechanical setting is strictly isometric: there is no ventricular geometry, preload/afterload, or closed-loop circulation, and no pressure–volume loops are represented. Accordingly, results are reported in terms of tension-derived biomarkers (e.g., ATpeak, ATmin, DevF, TTP, RT50) rather than hemodynamic indices.

Remodeling scope. HFrEF remodeling is represented through literature-derived cellular proxies implemented as targeted modifications of ionic currents, Ca^{2+}-handling fluxes, and coupling-related parameters. System-level neurohumoral regulation and multi-scale feedback (e.g., autonomic tone, circulating hormones, long-term structural adaptation) are outside the scope.

Within these boundaries, the framework is designed to quantify how targeted cellular remodeling alters electrical, Ca^{2+}-handling, and mechanical biomarkers in a controlled *in silico* setting.

1.5 Thesis outline

Chapter 2 presents the aim of the work and the specific objectives. Chapter 3 describes the computational framework, pacing protocol, remodeling implementation, and biomarker extraction pipeline. Chapter 4 reports the effects of HFrEF remodeling on electrophysiological, Ca^{2+}-handling, and mechanical biomarkers, including sensitivity and convergence analyses where applicable. Chapter 5 summarizes limitations of the single-cell approach and outlines directions for future work. Finally, Chapter 6 interprets the results mechanistically and compares trends against the literature reference.

Chapter 2

Thesis Objectives

The aim of this thesis is to characterize the single-cell HFrEF remodeling signature in a human ventricular electromechanical model by implementing a literature-informed HFrEF configuration in BPSLand [6] and quantifying its effects through a standardized set of electrophysiological, Ca^{2+}-handling, and mechanical biomarkers. Literature-based targets and expected trend directions are taken from Mora *et al.* as an external reference [3].

Accordingly, the objectives are:

- Establish a CTRL baseline in BPSLand and verify steady-state behavior under the chosen pacing protocol [6].
- Define HFrEF remodeling targets (ionic, Ca^{2+}-cycling, and dyadic/structural proxies) from the reference framework and supporting literature [3].
- Implement the selected targets in BPSLand in a modular manner to enable controlled activation/deactivation of remodeling components.
- Quantify CTRL vs. HFrEF differences using a predefined biomarker set spanning AP repolarization (APD_{50}, APD_{90}), CaT magnitude/kinetics, and tension-based indices.
- Compare simulated HF/CTRL trends against the reference expectations to assess cross-domain consistency and physiological plausibility [3].

Chapter 3

Materials and Methods

This chapter outlines the computational protocol used to simulate CTRL and HFrEF conditions with the BPSLand human ventricular cardiomyocyte model and to extract steady-state biomarkers from the resulting waveforms. Remodeling settings, pacing/solver configuration, and biomarker definitions are specified for reproducibility of the Chapter 4 analyses. The workflow is shown in Fig. 3.1.

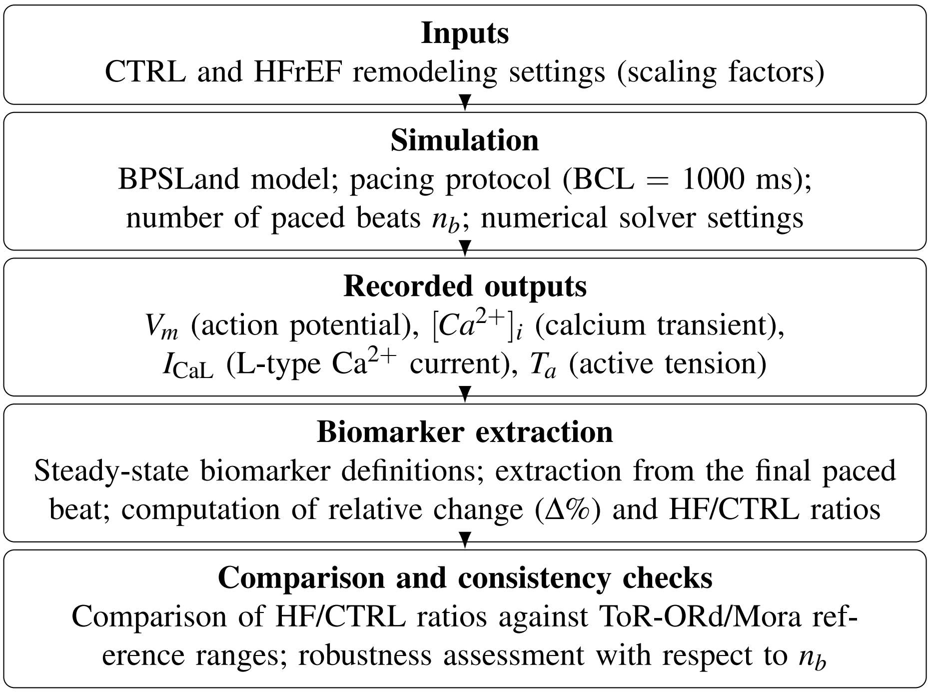

Figure 3.1: BPSLand simulation and biomarker analysis pipeline.

3.1 Remodeling parameter set and implementation mapping

This section describes how the HFrEF phenotype is implemented in the BPSLand framework through a compact set of remodeling scalings. We first outline the scaling strategy and the targeted mechanisms, and then report the CTRL and HFrEF parameter sets used throughout the simulations.

3.1.1 Overview of the remodeling implementation

To represent the HFrEF phenotype within the BPSLand electromechanical model, we apply a compact set of multiplicative scaling factors to selected transmembrane currents, Ca^{2+}-handling pathways, and SR-release control terms. This approach preserves the original model structure while enabling a controlled, component-wise implementation of literature-driven remodeling effects and their coupled impact on electrophysiological, Ca^{2+}-transient, and force-related outputs [3].

3.1.2 Remodeling targets and parameter meaning

The remodeling parameter set is organized into three functional groups, targeting membrane electrophysiology, Ca^{2+} handling, and SR release/trigger effectiveness. Remodeling is implemented through multiplicative scaling factors applied either to current/flux amplitudes or to kinetic time constants, without altering the underlying ODE structure of the BPSLand model [3].

(i) Sarcolemmal electrophysiology (inward/outward current balance and repolarization).

- **Late sodium current (I_{NaL}).** Multiplicative scaling of the *maximal conductance* (current amplitude) of the late Na^+ current during the plateau, which reduces repolarization reserve and tends to prolong APD.

- **Late sodium inactivation time constant (τ_{hL}).** Multiplicative scaling of the I_{NaL} inactivation time constant, altering the kinetics of late Na^+ current decay and therefore its persistence during repolarization.

- **Transient outward potassium current (I_{to}).** Multiplicative scaling of the *maximal conductance* of I_{to}, shaping early repolarization (phase 1) and influencing notch depth and plateau level.

- **Inward rectifier potassium current (I_{K1}).** Multiplicative scaling of the *maximal conductance* of I_{K1}, affecting terminal repolarization and stabilizing the resting membrane potential.

- **Na^+/K^+ pump (I_{NaK}).** Multiplicative scaling of the *maximal pump current* of I_{NaK}, influencing ionic homeostasis and indirectly modulating repolarization robustness.

- **Na^+/Ca^{2+} exchanger (NCX).** Multiplicative scaling of the *maximal exchanger current* of NCX, an electrogenic sarcolemmal transporter that links Ca^{2+} extrusion to membrane voltage through its contribution to the total membrane current.

- **L-type Ca^{2+} channel amplitude (bG_{CaL}).** Multiplicative scaling of the L-type channel current amplitude applied consistently to the Ca^{2+}, Na^+, and K^+ components (I_{CaL}, I_{CaNa}, I_{CaK}). This parameter effectively rescales the maximal L-type channel conductance/permeability and therefore modulates Ca^{2+} entry and the plateau current balance.

(ii) Intracellular Ca^{2+} handling and SR cycling (uptake, leak, release control, and regulation).

- **CaMKII activity** ($\mathrm{CaMK_a}$)**.** Multiplicative scaling of CaMKII-dependent modulation terms in the Ca^{2+} handling subsystem, representing altered phosphorylation-driven regulation under HFrEF conditions.

- **SERCA uptake (SERCA).** Multiplicative scaling of the *maximal SR uptake flux* J_{up} (SERCA strength), which shapes CaT decay and SR refilling.

- **SR leak (J_{leak}).** Multiplicative scaling of the *leak flux amplitude* from SR to cytosol, influencing SR Ca^{2+} load and diastolic Ca^{2+} levels.

- **SR release Ca^{2+}-dependence ($K_{\mathrm{rel,Ca}}$).** Scaling of the Ca^{2+}-dependence (sensitivity/gating) in the RyR-mediated release formulation, modulating the effective release gain.

- **SR release coefficient ($J_{\mathrm{rel\_cof}}$).** Multiplicative scaling of the *release flux amplitude* (effective release strength), providing a compact control of SR Ca^{2+} release.

3.1.3 Control and HFrEF scaling sets

Two parameter sets are used throughout this thesis. The control condition uses unity scaling for all targets, whereas the HFrEF condition applies the literature-informed scaling values reported below. For clarity and reproducibility, Table 3.1 summarizes the scaling factors used for both conditions.

Table 3.1: Scaling factors used to implement Control and HFrEF conditions in the BPS-Land framework.

Remodeling target	**Control**	**HFrEF**
I_{NaL}	1.00	1.30
τ_{hL}	1.00	1.80
I_{to}	1.00	0.40
I_{K1}	1.00	0.68
I_{NaK}	1.00	0.80
NCX	1.00	1.40
CaMK_a	1.00	1.40
SERCA	1.00	0.77
J_{leak}	1.00	1.31
$K_{\text{rel,Ca}}$	1.00	0.59
$J_{\text{rel\_cof}}$	1.00	0.54
bG_{CaL}	1.00	0.70

In subsequent analyses, these remodeling factors define the *only* differences between baseline and HFrEF simulations at the model-parameter level; protocol details (pacing, steady-state enforcement, and numerical settings) are reported separately in the simulation setup section.

3.2 Biomarker definitions and extraction

To quantify baseline and HFrEF-remodeled behavior, biomarkers are extracted from simulated traces of transmembrane potential $V_m(t)$, cytosolic calcium concentration $[Ca^{2+}]_i(t)$, and active tension $T(t)$ on the final paced beat at steady state. A subset of biomarkers is directly comparable to the ToR-ORd/Mora reference (APD$_{90}$, systolic Ca^{2+}, CaT timing indices, and developed force), while additional readouts are reported for internal characterization of the BPSLand platform and to support interpretation when a one-to-one mapping to Mora outputs is not available[3].

Timing conventions and analysis window. Biomarkers are computed from the *final paced beat* after steady state is reached. Let t_0 denote the onset time of the stimulus current for the analyzed beat. Baseline values (e.g. $V_{\text{rest}}, Ca_{\text{diast}}$) are computed as averages over the pre-stimulus window $[t_0 - \Delta t_{\text{base}}, t_0)$. All peak/extrema operations (e.g. V_{peak}, Ca_{syst}, ATpeak/ATmin) are evaluated over the single-beat analysis interval $[t_0, t_0 + T_{\text{beat}}]$, with T_{beat} equal to the BCL in this work. The maximum upstroke velocity $\frac{dV_m}{dt}\Big|_{\max}$ is computed within the restricted window $[t_0, t_0 + \Delta t_{\text{up}}]$ to isolate phase-0 depolarization. For threshold-based timing metrics (APD and CaTD), the first threshold crossing is taken on the repolarization/decay branch, i.e. after the corresponding peak within the same beat.

3.2.1 Electrical biomarkers

Electrical remodeling is quantified primarily through APD$_{90}$, with APD$_{50}$ reported as a secondary index of early repolarization/plateau dynamics. Let t_0 denote the stimulus reference time for the analyzed beat, V_{rest} the baseline resting membrane potential, and V_{peak} the peak membrane potential.

- **Resting membrane potential (RMP).** Baseline membrane potential immediately prior to stimulation:

$$\text{RMP} = \overline{V_m(t)} \qquad \text{for } t \in [t_0 - \Delta t_{\text{base}}, t_0). \tag{3.1}$$

- **Peak membrane potential (V_{peak}).** Maximum membrane voltage after stimulation:

$$V_{\text{peak}} = \max_{t \in [t_0, t_0 + T_{\text{beat}}]} V_m(t). \tag{3.2}$$

- **Maximum upstroke velocity ($\frac{dV_m}{dt}\Big|_{\max}$).** Maximum time-derivative during the AP upstroke:

$$\left.\frac{dV_m}{dt}\right|_{\max} = \max_{t\in[t_0, t_0+\Delta t_{\text{up}}]} \frac{dV_m}{dt}(t). \tag{3.3}$$

- **APD$_{90}$ (primary electrical biomarker).** Action potential duration at 90% repolarization. Define the repolarization threshold:

  $$V_{90} = V_{\text{rest}} + 0.10\,(V_{\text{peak}} - V_{\text{rest}}). \tag{3.4}$$

  Let t_{90} be the first time on the repolarization phase such that $V_m(t_{90}) \leq V_{90}$. Then:

  $$\text{APD}_{90} = t_{90} - t_0. \tag{3.5}$$

- **APD$_{50}$ (secondary electrical biomarker).** Action potential duration at 50% repolarization. Define the threshold:

  $$V_{50} = V_{\text{rest}} + 0.50\,(V_{\text{peak}} - V_{\text{rest}}). \tag{3.6}$$

  With t_{50} the first repolarization time such that $V_m(t_{50}) \leq V_{50}$:

  $$\text{APD}_{50} = t_{50} - t_0. \tag{3.7}$$

3.2.2 Calcium-handling biomarkers

Calcium-handling remodeling is quantified using cytosolic Ca^{2+} transient (CaT) amplitude and timing indices. Let $[Ca^{2+}]_i(t)$ denote cytosolic calcium concentration for the analyzed beat.

- **Diastolic Ca^{2+} (Ca_{diast}).** Baseline cytosolic Ca^{2+} immediately prior to stimulation:

  $$Ca_{\text{diast}} = \overline{[Ca^{2+}]_i(t)} \qquad \text{for } t \in [t_0 - \Delta t_{\text{base}}, t_0). \tag{3.8}$$

- **Systolic Ca^{2+} (Ca_{syst}).** Peak cytosolic Ca^{2+} after stimulation:

  $$Ca_{\text{syst}} = \max_{t\in[t_0, t_0+T_{\text{beat}}]} [Ca^{2+}]_i(t). \tag{3.9}$$

- **Time-to-peak CaT (TTP).** Time from stimulus to peak Ca^{2+}:

  $$\text{TTP}_{Ca} = t_{\text{peak},Ca} - t_0, \qquad t_{\text{peak},Ca} = \arg\max [Ca^{2+}]_i(t). \tag{3.10}$$

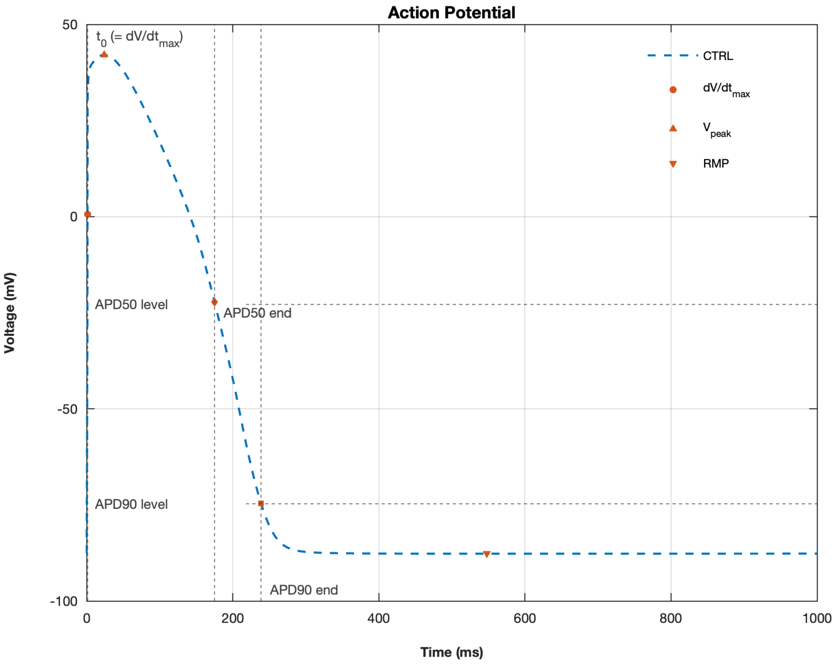

Figure 3.2: Action potential biomarkers: RMP, V_{peak}, APD_{50}, APD_{90}.

- **CaT relaxation time $\mathbf{RT_{50}}$ (RT50).** Time from Ca^{2+} peak to 50% recovery:

  $$Ca_{50} = Ca_{\text{diast}} + 0.50\,(Ca_{\text{syst}} - Ca_{\text{diast}}). \tag{3.11}$$

  Let $t_{50,Ca}$ be the first decay time such that $[Ca^{2+}]_i(t_{50,Ca}) \leq Ca_{50}$. Then:

  $$\text{RT}_{50,Ca} = t_{50,Ca} - t_{\text{peak},Ca}. \tag{3.12}$$

- **$\mathbf{CaTD_{50}}$ and $\mathbf{CaTD_{90}}$.** CaT "duration" at 50% and 90% recovery (from stimulus time):

  $$\begin{aligned} Ca_{50} &= Ca_{\text{diast}} + 0.50\,(Ca_{\text{syst}} - Ca_{\text{diast}}), \\ Ca_{90} &= Ca_{\text{diast}} + 0.10\,(Ca_{\text{syst}} - Ca_{\text{diast}}). \end{aligned} \tag{3.13}$$

  With $t_{x,Ca}$ the first decay time such that $[Ca^{2+}]_i(t_{x,Ca}) \leq Ca_x$ on the decay phase:

  $$\begin{aligned} \text{CaTD}_{50} &= t_{50,Ca} - t_0, \\ \text{CaTD}_{90} &= t_{90,Ca} - t_0. \end{aligned} \tag{3.14}$$

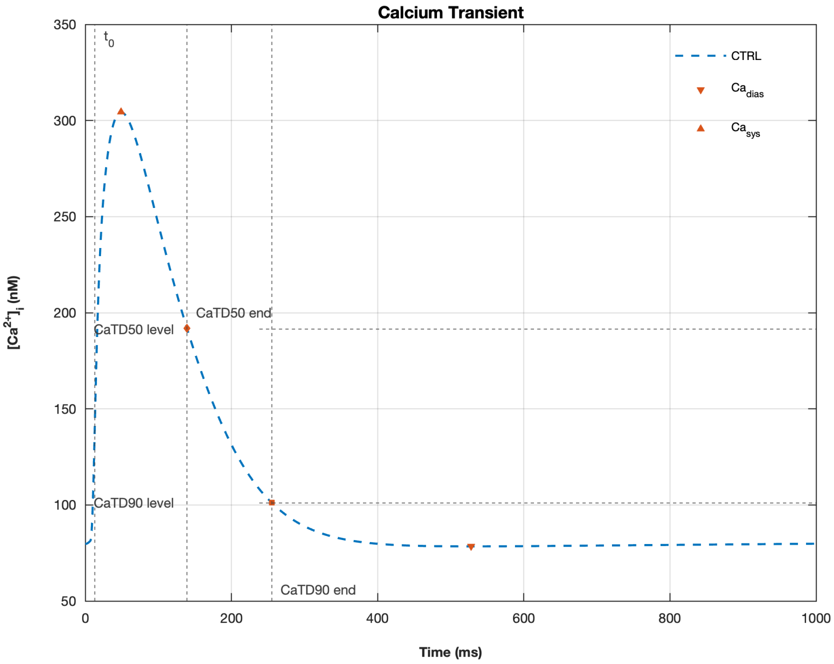

Figure 3.3: Calcium-transient biomarkers: Ca_{diast}, Ca_{syst}, TTP_{Ca}, $\text{RT}_{50,Ca}$, $CaTD_{50}$, $CaTD_{90}$.

3.2.3 Mechanical biomarker

Mechanical consequences of remodeling are summarized using tension-derived biomarkers computed from the active tension trace $T_a(t)$ over a single beat. The stimulus reference time t_0 denotes the onset of the applied stimulus for the analyzed beat.

- **Minimum active tension (ATmin).** Minimum value of the active tension trace over the beat:

$$\text{ATmin} = \min_{t\in[t_0,t_0+T_{\text{beat}}]} T_a(t). \tag{3.15}$$

- **Peak active tension (ATpeak).** Maximum value of the active tension trace over the beat:

$$\text{ATpeak} = \max_{t\in[t_0,t_0+T_{\text{beat}}]} T_a(t). \tag{3.16}$$

- **Developed force (DevF).** Beat-to-beat developed force amplitude:

$$\text{DevF} = \text{ATpeak} - \text{ATmin}. \tag{3.17}$$

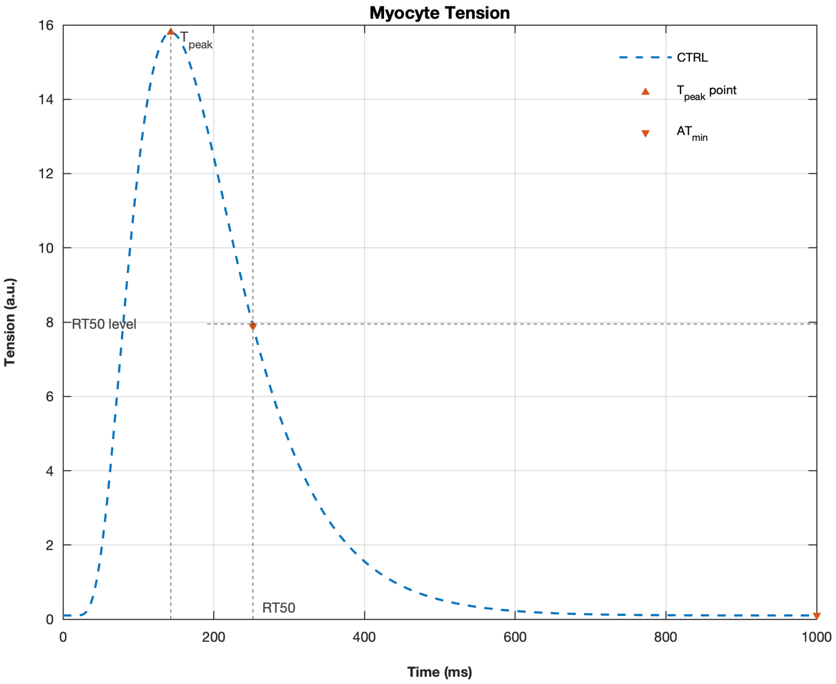

Figure 3.4: Graphical definition of active-tension biomarkers (ATmin, ATpeak, DevF, TTP_T, $\mathrm{RT50}_T$*) extracted from the final paced beat at steady state.*

- **Time to peak (TTP).** Time from stimulus onset to peak tension:

$$\mathrm{TTP} = t_{\mathrm{peak}} - t_0, \qquad t_{\mathrm{peak}} = \arg \max_{t \in [t_0, t_0 + T_{\mathrm{beat}}]} T_a(t). \tag{3.18}$$

- **Relaxation time at 50% ($\mathbf{RT50}_T$).** Time from peak tension to 50% relaxation of the developed component:

$$T_{50} = \mathrm{ATmin} + 0.5\,(\mathrm{ATpeak} - \mathrm{ATmin}), \qquad \mathrm{RT50}_T = t_{50} - t_{\mathrm{peak}}, \tag{3.19}$$

  where t_{50} is the first time after t_{peak} such that $T_a(t_{50}) \leq T_{50}$ within the same beat.

3.2.4 Extraction rules and conventions

All biomarkers are computed on the final beat after steady state is reached (steady-state criteria and pacing protocol are reported in Chapter 4 simulation setup). The stimulus reference time t_0 is defined as the onset of the applied stimulus current for the analyzed beat. Baseline quantities (V_{rest}, Ca_{diast}, T_{diast}) are computed as averages over a pre-stimulus window of duration Δt_{base} immediately preceding t_0. APD and CaTD metrics are computed using beat-specific thresholds defined relative to the corresponding baseline and peak values of the same beat, ensuring robustness to baseline shifts under remodeling. Unless stated otherwise, no smoothing or filtering is applied prior to biomarker extraction. In particular, $dV/dt_{\max}$ is reported in mV/ms (equivalent to V/s), and tension outputs (ATpeak/ATmin/DevF) are reported in the model tension unit (kPa in this work).

Reported units follow the model outputs (ms for time, mV for V_m, concentration units for $[Ca^{2+}]_i$, and model tension units for T).

3.3 Simulation environment and numerical protocol (MATLAB)

All simulations were executed in MATLAB using the BPSLand electromechanical model under periodic pacing. This section summarizes the numerical configuration, pacing protocol, and the main output signals stored for biomarker extraction and reporting.

3.3.1 Software and solver settings

Simulations were performed in MATLAB by integrating the coupled ODE system with the stiff solver `ode15s`. The integration step was constrained to `MaxStep`=1 ms to ensure consistent temporal resolution for waveform-based biomarker extraction [35, 36]. This corresponds to the solver option `options = odeset('MaxStep',1)` used in the simulation script.

Solver tolerances were not explicitly set in the code; therefore `ode15s` default tolerances of the installed MATLAB version were used (`RelTol` and `AbsTol` at default values). All simulations (CTRL and HFrEF) used the same solver configuration and settings.

3.3.2 Pacing protocol and steady-state criteria

Cells were paced periodically with basic cycle length BCL = 1000 ms (1 Hz). The stimulus was applied as a rectangular current pulse at the beginning of each cycle with amplitude -53 μA/μF and duration 1 ms (current-clamp pacing). For each condition (CTRL and HFrEF), the model was simulated for n_b beats starting from the same initial-state vector loaded from `InitialConditions`, and biomarkers were computed from the final paced beat.

To assess that the extracted biomarkers were not sensitive to the selected run length, simulations were repeated with $n_b = \{200, 300, 500\}$ beats at fixed BCL $=$ 1000 ms; the corresponding robustness analysis is reported in Section 4.1.

3.3.3 Recorded outputs and data organization

For each condition, state variables were simulated over all beats and the final-beat state trajectory was retained for biomarker extraction. The primary stored waveforms were transmembrane potential V_m, intracellular calcium $[Ca^{2+}]_i$, SR calcium $[Ca^{2+}]_{\mathrm{SR}}$, and active tension T_a.

In addition to state variables, ionic currents and Ca^{2+}-handling fluxes were evaluated by re-calling the model right-hand side along the stored trajectory and saved as structured outputs. In particular, the last-beat current set included I_{Na}, I_{NaL}, I_{to}, I_{CaL}, I_{Kr}, I_{Ks}, I_{K1}, I_{NaCa} (subspace and bulk components), and I_{NaK}, together with SR flux terms such as release and uptake (e.g., J_{rel}, J_{up}), as required for mechanistic interpretation.

All outputs were stored in consistent data structures across CTRL and HFrEF (state variables and last-beat currents), enabling matched biomarker extraction from identical signal definitions.

The final set reported in Table 3.1 represents the exact parameter multipliers used in the simulations.

Chapter 4

Results and Discussion

This chapter reports steady-state CTRL and HFrEF simulations obtained with the BPSLand electromechanical model and summarizes remodeling effects using waveform- and biomarker-level comparisons.

4.1 Robustness to number of paced beats

Before presenting the main results, we verified that the reported steady-state waveforms and biomarkers are not sensitive to the length of preconditioning. All simulations were repeated under identical protocol settings (BCL = 1000 ms), varying only the number of paced beats $n_b \in \{200, 300, 500\}$, and biomarkers were computed from the final paced beat. Because HF/CTRL biomarker ratios changed only marginally across this range (Table 4.1), the remainder of this chapter reports results from $n_b = 500$ to provide a conservative steady-state margin and minimize residual transient effects.

Figures 4.1–4.4 overlay the main waveforms (action potential, Ca^{2+} transient, I_{CaL}, and active tension) obtained at $n_b = 200$, 300, and 500 for both CTRL and HFrEF, showing that the traces are visually stable with increasing n_b. Quantitatively, Table 4.1 reports percent differences of HF/CTRL ratios between n_b settings (200→300, 300→500, and 200→500), computed as $\Delta\% = 100\,(R_2 - R_1)/R_1$, where R denotes the HF/CTRL ratio.

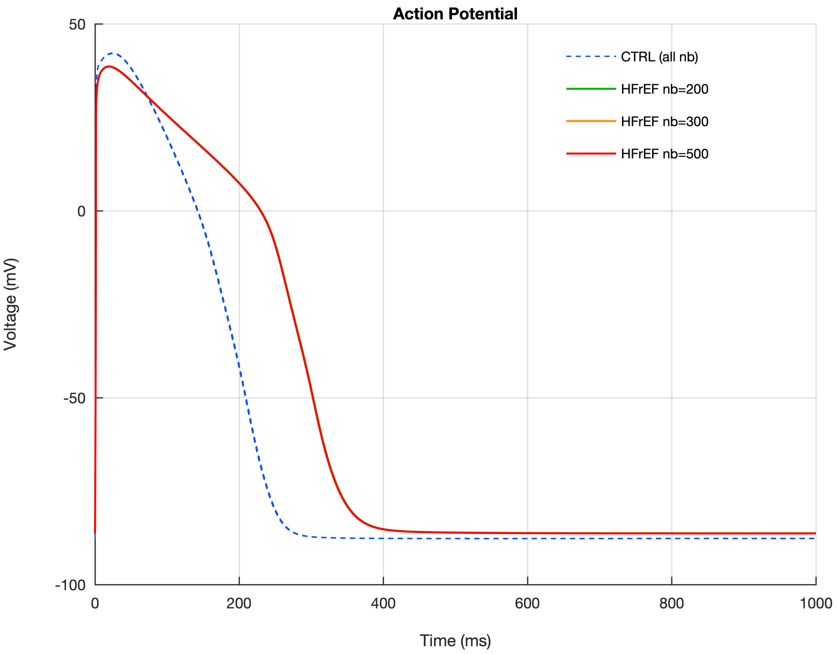

Figure 4.1: Action potential waveforms at $n_b = 200$, 300, and 500 (CTRL and HFrEF; BCL $= 1000$ ms).

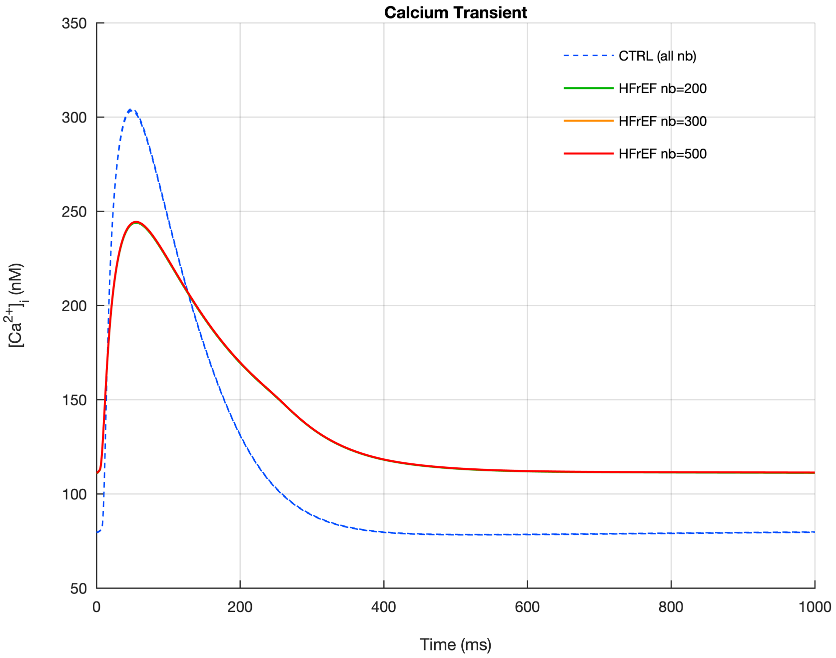

Figure 4.2: Intracellular Ca^{2+} transient at $n_b = 200$, 300, and 500 (CTRL and HFrEF).

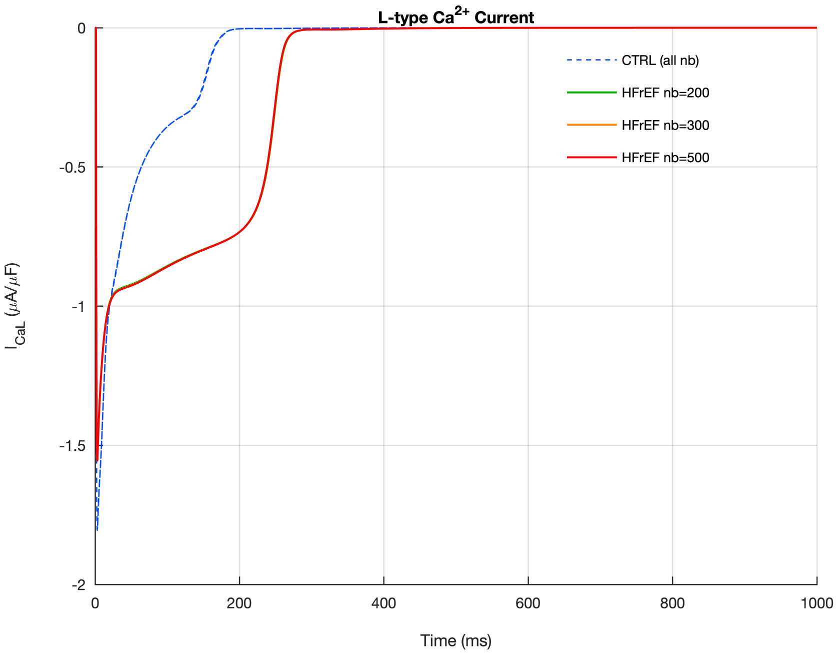

Figure 4.3: L-type Ca^{2+} current I_{CaL} at $n_b = 200$, 300, and 500 (CTRL and HFrEF).

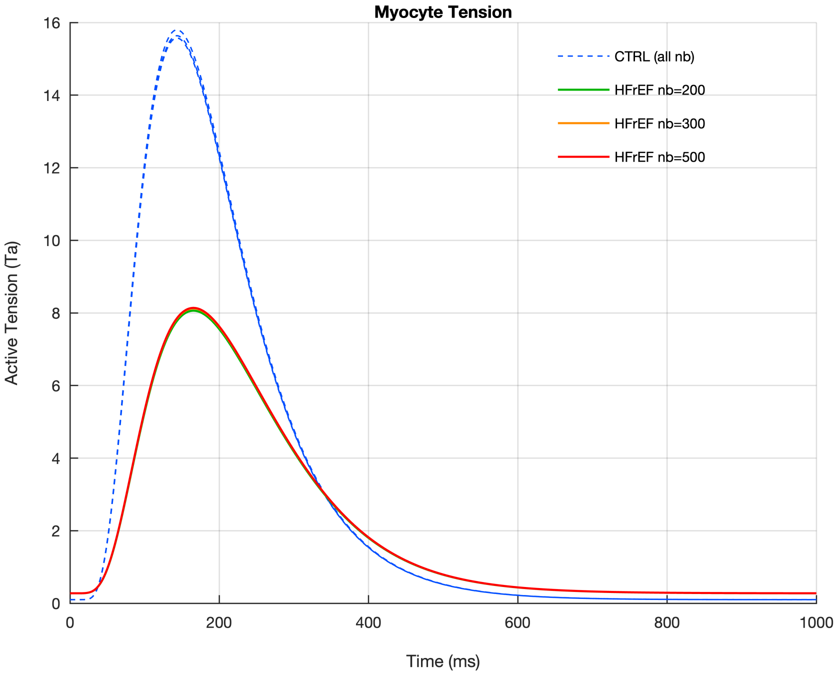

Figure 4.4: Active tension at $n_b = 200$, 300, and 500 (CTRL and HFrEF).

Biomarker	**Δ% 200→300**	**Δ% 300→500**	**Δ% 200→500**	**Max $\|\Delta\%\|$**
APD90 (ms)	-0.20	-0.20	-0.40	0.40
CaSyst (nM)	0.20	0.10	0.30	0.30
TTP (ms)	0.90	0.40	1.30	1.30
RT50 (ms)	-0.70	0.90	0.20	0.90
ATpeak	0.91	0.35	1.25	1.25
ATmin	0.74	0.36	1.10	1.10
DevF (kPa)	1.79	0.70	2.50	2.50
Vpeak (mV)	-0.30	-0.20	-0.50	0.50
RMP (mV)	0.00	0.10	0.10	0.10
APD50 (ms)	-0.60	-0.60	-1.20	1.20
dV/dtmax	0.00	0.00	0.00	0.00
CaDiast (nM)	0.40	0.20	0.60	0.60
CaTD50 (ms)	0.00	-0.60	-0.60	0.60
CaTD90	0.60	-0.10	0.50	0.60
Max across biomarkers	**1.79**	**0.90**	**2.50**	**2.50**

Table 4.1: Sensitivity of HF/CTRL biomarker ratios to the number of paced beats n_b.

Overall, HF/CTRL ratios showed limited sensitivity to n_b within the tested range (Table 4.1), supporting the use of $n_b = 500$ for steady-state reporting in the subsequent analyses. We used $n_b = 500$ paced beats, consistent with the steady-state protocol used in Mora *et al.* [3].

4.2 BPSLand Model Analysis

This section presents the steady-state CTRL and HFrEF waveforms produced by BPSLand (membrane voltage, Ca^{2+} transient, I_{CaL}, and active tension) to provide qualitative context for the biomarker-level comparisons reported in Section 4.3.

4.2.1 Action potential

Figure 4.5 compares the action potential waveforms for CTRL and HFrEF. The HFrEF trace exhibits delayed repolarization and a longer action potential duration, consistent with the biomarker analysis (APD_{90} HF/CTRL $= 1.40$, $\Delta = +40.0\%$). APD_{50} shows a concordant prolongation, indicating that the remodeling effect reflects a broader reduction in repolarization reserve.

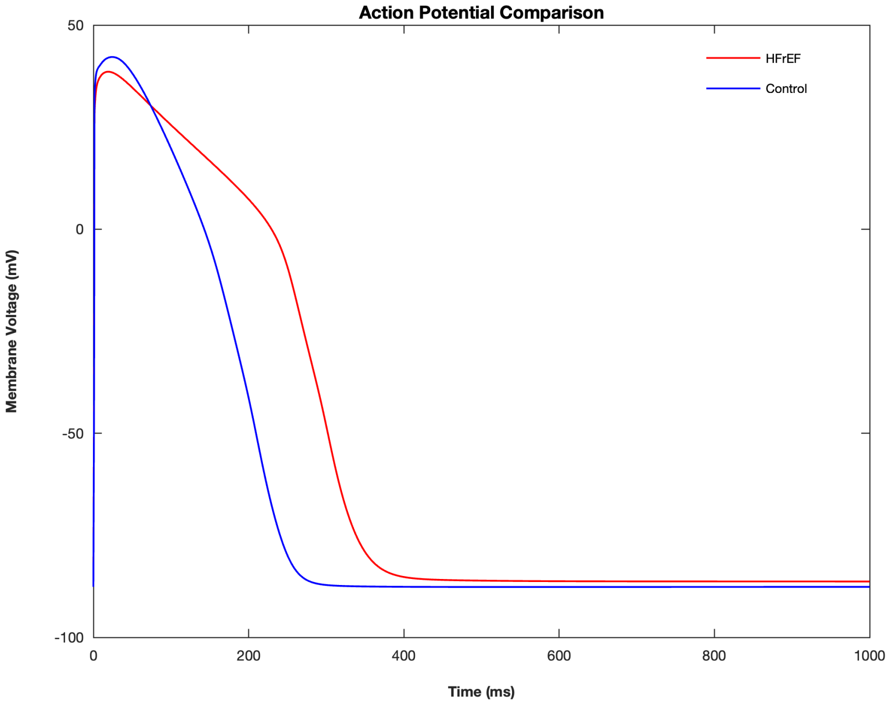

Figure 4.5: Action potential waveforms for CTRL and HFrEF conditions (BPSLand model; BCL $= 1000$ ms*).*

In the present HFrEF parameterization (Table 3.1), APD prolongation is primarily driven by a reduced repolarization reserve due to downscaling of outward K^+ currents (notably I_{to} and I_{K1}) together with an increased late inward contribution (I_{NaL} and slowed late inactivation, τ_{hL}). By contrast, the maximal I_{CaL} conductance is reduced ($bG_{\mathrm{CaL}} < 1$), so the longer plateau arises from the net current balance rather than from an increased I_{CaL} magnitude. An extended plateau also alters the voltage-time window that shapes both Ca^{2+} entry through I_{CaL} and the electrogenic contribution of NCX, supporting a coupled EP–Ca^{2+} interpretation of the phenotype [7, 29, 3].

4.2.2 Calcium transient

Figure 4.6 compares the intracellular Ca^{2+} transients for CTRL and HFrEF. Relative to CTRL, HFrEF exhibits reduced systolic Ca^{2+} and elevated diastolic Ca^{2+}, together with slower decay kinetics. This is quantified in Section 4.3: CaSyst decreases (HF/CTRL $= 0.59$, $\Delta = -40.9\%$), CaDiast increases (HF/CTRL $= 1.42$, $\Delta = +42.3\%$), and $CaTD_{90}$ is prolonged (HF/CTRL $= 1.38$, $\Delta = +37.8\%$).

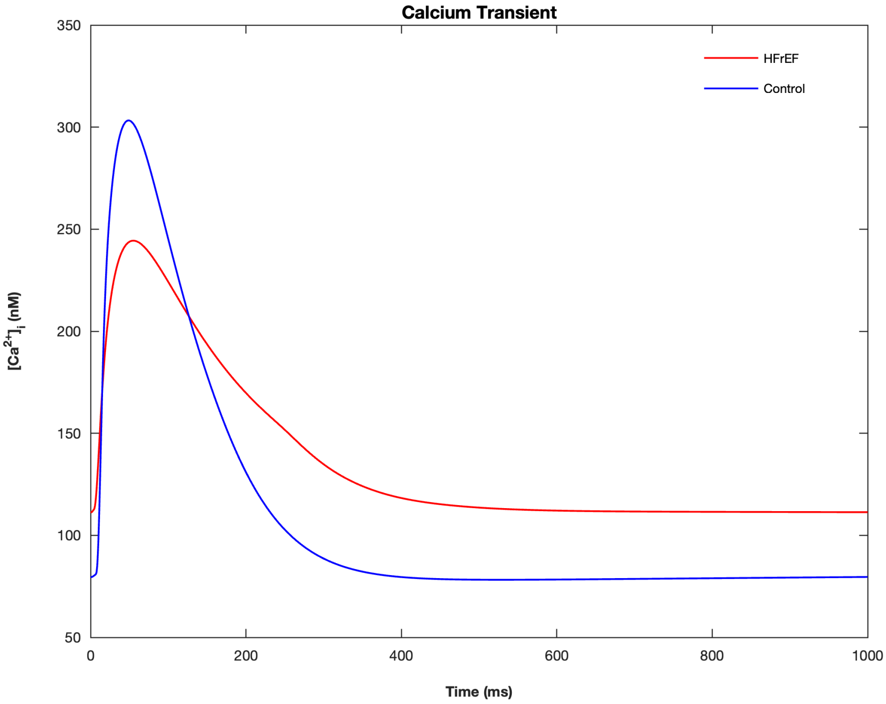

Figure 4.6: Intracellular Ca^{2+} transient for CTRL and HFrEF conditions (BPSLand).

The remodeled Ca^{2+} phenotype is coherent with impaired Ca^{2+} cycling, where systolic and diastolic levels reflect the balance between SR uptake (SERCA), SR release (RyR-mediated J_{rel}), SR leak, and sarcolemmal extrusion via NCX [20, 21]. In the present HFrEF configuration, reduced SERCA activity and altered release/leak parameters (Table 3.1) promote lower SR Ca^{2+} content and smaller peak release while slowing cytosolic Ca^{2+} removal, providing a mechanistic explanation for reduced CaSyst, increased CaDiast, and prolonged decay [27, 3]. Because trigger influx occurs via I_{CaL} during the action-potential plateau, the electrical remodeling shown in Figure 4.5 is expected to further modulate Ca-induced Ca release and the resulting Ca^{2+} transient [24].

4.2.3 L-type Ca^{2+} current (I_{CaL})

Figure 4.7 shows the L-type Ca^{2+} current traces for CTRL and HFrEF. Differences in the I_{CaL} time course reflect changes in trigger Ca^{2+} entry during the action-potential plateau and provide a direct link between the voltage phenotype and Ca^{2+} cycling [7, 5]. In the remodeled condition, I_{CaL} is shaped jointly by (i) the imposed conductance scaling (bG_{CaL} in Table 3.1) and (ii) altered channel gating driven by the different plateau voltage trajectory and by Ca-dependent inactivation (CDI) through the modified Ca^{2+} transient [5, 6].

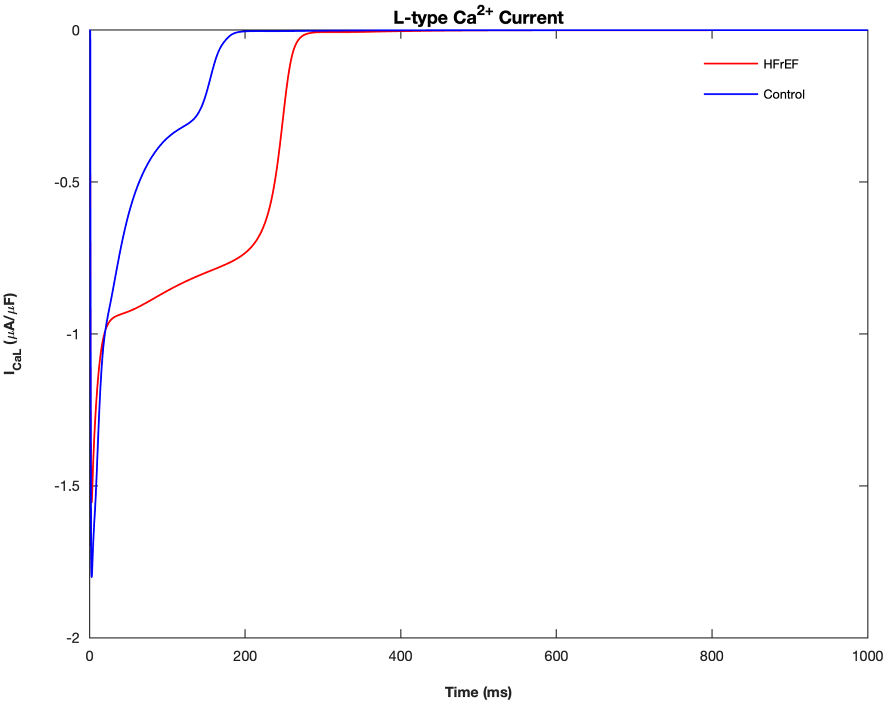

Figure 4.7: L-type Ca^{2+} current (I_{CaL}) for CTRL and HFrEF conditions (BPSLand).

A longer plateau can shift the timing and extent of both voltage-dependent and Ca-dependent inactivation of I_{CaL} [7, 5]. Consequently, even with a reduced maximal conductance, the net Ca^{2+} entry profile can change in a way that affects SR release triggering and contributes to the altered Ca^{2+} transient amplitude and kinetics observed in Figure 4.6 and quantified in Section 4.3.

4.2.4 Myocyte tension

Figure 4.8 shows the active tension (T_a) traces for CTRL and HFrEF. Relative to CTRL, the HFrEF simulation exhibits a marked reduction in peak active tension together with a slower contraction–relaxation profile. This behavior is consistent with the Ca^{2+} handling changes reported above: reduced systolic Ca^{2+} decreases myofilament activation, while prolonged Ca^{2+} removal delays relaxation [20, 6].

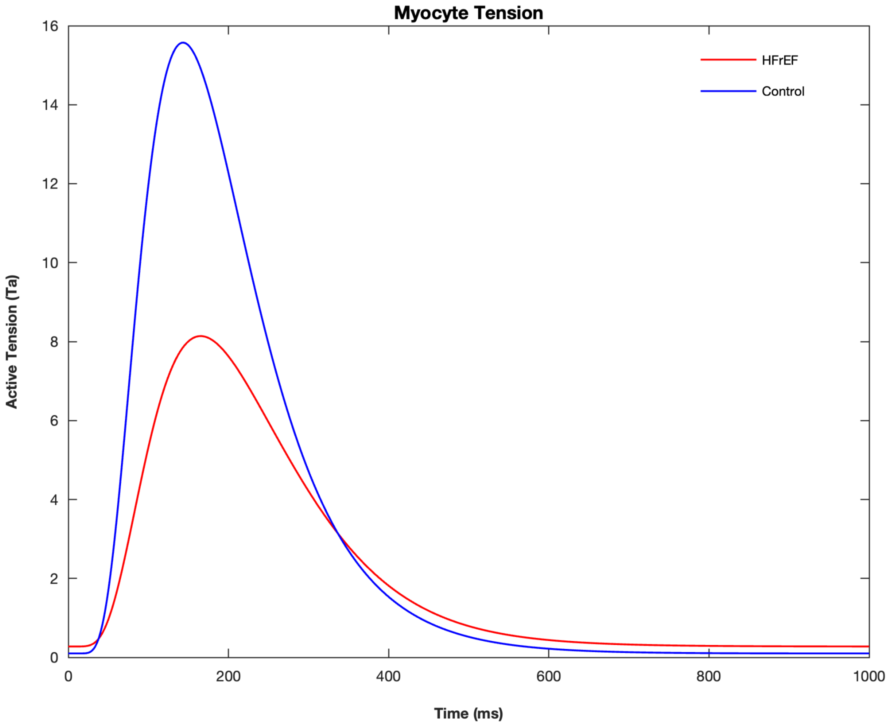

Figure 4.8: Active tension traces for CTRL and HFrEF conditions (BPSLand).

This is reflected in tension-derived biomarkers (Section 4.3): ATpeak decreases substantially (HF/CTRL $= 0.52$, $\Delta = -47.7\%$) while ATmin increases (HF/CTRL $= 2.75$), indicating higher residual/diastolic active tension. Developed force (DevF $=$ ATpeak$-$ATmin) is also reduced (HF/CTRL $= 0.51$). Timing indices (TTP and RT50) show smaller relative changes, consistent with waveform kinetics being more sensitive to model-specific coupling and biomarker definitions than amplitude-based markers [10, 9].

4.3 Biomarker analysis

This section quantifies CTRL vs. HFrEF differences using steady-state biomarkers extracted from the final paced beat ($n_b = 500$, BCL = 1000 ms). For each biomarker, absolute values are reported for both conditions together with the percent change ($\Delta\%$) and the HF/CTRL ratio. For mechanical output, ATpeak and ATmin denote the peak and diastolic active tension of the last paced beat, and developed force is defined as DevF = ATpeak − ATmin.

4.3.1 Key biomarkers with experimental HF/CTRL ranges

Table 4.2 reports a subset of biomarkers for which experimental HF/CTRL ranges are available in the literature ("Experimental range" column). For completeness, the corresponding ToR-ORd–based HF/CTRL ratios reported by Mora [3] are also included as a simulation-based reference.

BPSLand reproduces the expected qualitative electrical and Ca^{2+} remodeling: APD_{90} is prolonged (HF/CTRL = 1.40, $\Delta = +40.0\%$) and CaSyst is reduced (HF/CTRL = 0.59, $\Delta = -40.9\%$). For APD_{90}, the BPSLand ratio is close to the Mora value (1.54) and lies within the reported experimental range. For CaSyst, the BPSLand ratio matches the Mora trend (0.60) and is close to the experimental range.

For contractile kinetics, BPSLand predicts increases in TTP and RT50 (HF/CTRL = 1.16 and 1.24). These ratios are closer to the available experimental ranges than the larger increases reported by Mora (1.41 and 1.53), suggesting that tension timing indices may be particularly sensitive to the specific electromechanical coupling formulation and biomarker definitions [10, 9].

Biomarker	**CTRL**	**HFrEF**	**Δ%**	**BPS HF/CTRL**	**Mora HF/CTRL**	**Experimental range**
APD90 (ms)	239.6	335.5	40.0	1.40	1.54	1.16–1.46 [44, 45]
CaSyst (nM)	225	133	-40.9	0.59	0.60	0.50–0.56 [39, 46]
TTP (ms)	142.9	165.6	15.9	1.16	1.41	0.99–1.14 [42, 43]
RT50 (ms)	107.6	133.8	24.4	1.24	1.53	1.10–1.11 [40, 41]
DevF (kPa)	15.47	7.86	-49.2	0.51	0.60	0.52–0.88 [41, 47]

Table 4.2: Key biomarkers for which experimental HF/CTRL ranges are available.

4.3.2 Additional model-based biomarkers (cross-model comparison)

Table 4.3 reports additional electrophysiological, Ca^{2+}-handling, and tension-related biomarkers computed from the BPSLand simulations at steady state. For these biomarkers, experimental HF/CTRL ranges are not reported consistently in the literature; therefore the "Mora HF/CTRL" column is used as a ToR-ORd–based cross-model reference rather than an experimental validation target [3].

Across most indices, BPSLand and the Mora/ToR-ORd reference show consistent qualitative remodeling trends. APD_{50} prolongs in the remodeled condition (HF/CTRL = 1.53), consistent with the APD_{90} prolongation. Ca^{2+} handling also remodels directionally as expected, with elevated CaDiast (HF/CTRL = 1.42) and slower decay ($CaTD_{90}$ HF/CTRL = 1.38). The smaller CaTD prolongation in BPSLand compared with Mora (1.38 vs. 1.96) indicates that late Ca^{2+} removal dynamics are particularly model-dependent and sensitive to parameter mapping choices.

A useful interpretation point is the link between the final BPSLand remodeling scalings (Table 3.1) and the Mora ToR-ORd targets (Table 1.1). While Mora provides remodeling directions and magnitudes in a different ionic framework, the BPSLand mapping required tuning of the corresponding targets (e.g., repolarizing K^+ currents, late inward currents, and SR release/uptake-related parameters) to produce a coherent HFrEF signature in this electromechanical model. This highlights that quantitative HF/CTRL ratios can depend on the specific model formulation, and that different models may emphasize different "leverage points" (e.g., repolarization reserve vs. trigger Ca^{2+} entry vs. SR flux balance) when reproducing the same high-level HFrEF phenotype.

Biomarker	**CTRL**	**HFrEF**	**Δ%**	**BPS HF/CTRL**	**Mora HF/CTRL**
Vpeak (mV)	42.19	38.58	-8.60	0.91	0.88
RMP (mV)	-87.66	-86.31	-1.50	0.98	0.99
APD50 (ms)	175.86	268.60	52.70	1.53	1.69
dV/dtmax (mV/ms)	248.81	222.44	-10.60	0.89	0.88
CaDiast (nM)	78.23	111.3	42.30	1.42	1.37
CaTD90 (ms)	251.41	346.45	37.80	1.38	1.96
CaTD50 (ms)	138.86	180.60	30.10	1.30	2.05
ATpeak (kPa)	15.57	8.14	-47.70	0.52	0.62
ATmin (kPa)	0.11	0.28	175.3	2.75	2.53

Table 4.3: BPSLand model-derived biomarkers for CTRL and HFrEF.

Chapter 5

Limitations and Future Work

This thesis provided a controlled, quantitative comparison of CTRL and HFrEF remodeling in a single-cell setting using the BPSLand human ventricular electromechanical model. The simulations reproduced coherent HFrEF-associated signatures in repolarization and Ca^{2+} cycling, but several limitations constrain interpretation and generalizability.

Model dependence and parameter-mapping uncertainty. The findings depend on the specific ionic, Ca^{2+}-handling, and myofilament formulations in BPSLand, as well as on the adopted HFrEF scaling set and pacing protocol [6, 10]. In addition, the HFrEF configuration required mapping literature-based remodeling targets (derived in other ionic frameworks) onto BPSLand parameters; this mapping is not unique and can change which mechanisms dominate a given phenotype. Accordingly, the results should be read primarily as *relative* remodeling signatures (HF/CTRL ratios and $\Delta\%$) under a fixed protocol, rather than as absolute agreement with experimental or clinical measurements. Quantitative matching would require additional calibration and, ideally, data-constrained personalization and/or multi-dataset fitting [3, 19].

Biomarker definition and extraction sensitivity. Several biomarkers, particularly timing indices (e.g., time-to-peak and relaxation measures), depend on definition and post-processing choices. Reference event (stimulus vs. upstroke), baseline definition, smoothing/filters, normalization, and peak/threshold detection rules can all produce non-trivial differences, especially when comparing outputs obtained with different models or toolchains [3, 19]. A clear next step is to formalize biomarker definitions in a model-agnostic specification and apply a single standardized extraction workflow for cross-model analyses.

Mechanical phenotype: coupling assumptions and missing subcellular remodeling. The most specific limitation concerns mechanical readouts in cross-model benchmarking. While BPSLand produced plausible active-tension waveforms and captured the expected reduction in peak tension, agreement with the Mora/ToR-ORd reference was weaker for contraction and relaxation kinetics (e.g., TTP and RT50). This likely reflects differences in electromechanical coupling assumptions, parameter scalings, and biomarker conventions across modeling chains [10, 9]. Importantly, this thesis did *not* explicitly represent HFrEF-associated T-tubule dysregulation. Because T-tubule remodeling can alter the synchrony of Ca^{2+} release and slow force development and relaxation, its absence may contribute to discrepancies in tension kinetics and amplitude relative to frameworks that account for altered EC-coupling microstructure. Future work should therefore test sensitivity of tension biomarkers to Ca^{2+}-to-force coupling parameters and Ca^{2+} release dynamics, and benchmark against independent datasets reporting human ventricular contraction kinetics when available.

Protocol scope and rate dependence. All simulations were performed at a single pacing rate ($BCL = 1000$ ms). Since rate dependence influences both electrical and Ca^{2+} phenotypes, extending the protocol to multiple cycle lengths would clarify which remodeling signatures persist across heart rates and which are rate-sensitive [7, 8]. This is particularly relevant for tension timing metrics and Ca^{2+} decay indices, which often show stronger frequency dependence than repolarization duration alone.

Richer phenotyping and uncertainty quantification. The analysis focused on waveform morphology and a core biomarker set. Extending the panel to include arrhythmia-relevant measures (e.g., repolarization-reserve proxies, alternans indicators, and triggers of abnormal depolarizations) would enable a more complete characterization than mean waveforms alone [29]. In addition, uncertainty quantification and parameter-variability analysis would move the comparison from single-point outputs to distributions, improving the robustness of conclusions based on HF/CTRL ratios [19].

Broader benchmarking. Finally, benchmarking should be broadened beyond a single reference study. Including additional published datasets and alternative ventricular model formulations would help separate remodeling signatures that are consistent across modeling assumptions from those that are formulation-dependent [21, 2].

Chapter 6

Conclusions

Heart failure with reduced ejection fraction (HFrEF) involves coordinated remodeling of ventricular electrophysiology, intracellular Ca^{2+} cycling, and contractile function. Human ventricular cardiomyocyte models provide a controlled framework to isolate these coupled mechanisms and to quantify remodeling through reproducible biomarkers. The aim of this thesis was to test whether the BPSLand human ventricular electromechanical model reproduces key cellular signatures of HFrEF, using a structured comparison against ToR-ORd–based HF/CTRL ratios reported by Mora et al. [3].

CTRL and HFrEF conditions were simulated under a fixed pacing protocol, using a consistent numerical configuration and a single post-processing pipeline to extract steady-state biomarkers from the final paced beat. This enabled coherent comparison at the waveform level (action potential, Ca^{2+} transient, I_{CaL}, and active tension) and at the biomarker level through HF/CTRL ratios and percent changes.

The simulations yielded a clear and internally consistent CTRL–HFrEF separation in electrophysiology and Ca^{2+} handling. In HFrEF, repolarization was prolonged and the plateau regime was altered, while Ca^{2+} cycling showed the expected combination of reduced systolic Ca^{2+}, elevated diastolic Ca^{2+}, and slower decay. These findings support a coupled interpretation in which the remodeled plateau is consistent with altered Ca^{2+} entry and Na^{+}/Ca^{2+} exchange contribution, contributing to downstream changes in Ca^{2+} transient amplitude and relaxation dynamics.

When compared with the Mora/ToR-ORd reference, BPSLand reproduced the expected direction of remodeling across the majority of biomarkers. Quantitative agreement was strongest for electrical indices and Ca^{2+} amplitude-related measures, while tension-kinetic biomarkers showed weaker agreement, highlighting the sensitivity of mechanical readouts to electromechanical coupling assumptions and to biomarker-definition choices across modeling pipelines [10, 9]. For biomarkers without direct experimental ranges in this work, Mora/ToR-ORd ratios were therefore used as a model-based reference for cross-model benchmarking rather than as experimental validation.

A robustness analysis with respect to the number of paced beats confirmed that extracted HF/CTRL ratios were only weakly sensitive to preconditioning length over $n_b \in \{200, 300, 500\}$, supporting that the reported remodeling signatures reflect stable steady-state behavior under the adopted protocol.

Overall, this thesis delivers a transparent and reproducible single-cell workflow to implement and analyze HFrEF remodeling in BPSLand. The study shows that BPSLand robustly captures the coupled electrical–Ca^{2+} phenotype of HFrEF under a fixed protocol, while identifying contraction kinetics as the main sensitivity point and a priority for future mechanical benchmarking and biomarker-standardization efforts.

Outlook and potential applications. Beyond benchmarking, the implemented HFrEF configuration can be used as an *in silico* testbed to probe mechanistic hypotheses and evaluate therapeutic strategies targeting specific pathways. For example, the model can quantify how interventions that (i) partially restore the downscaled repolarizing currents in this parameterization (e.g., I_{to}, I_{K1}), (ii) reduce late inward current (e.g., I_{NaL}), or (iii) improve Ca^{2+} cycling (e.g., SERCA function or SR leak/release balance) shift action potential duration, Ca^{2+} transient properties, and tension biomarkers toward CTRL ranges. Extending these tests across pacing rates and incorporating uncertainty analysis would strengthen the translational relevance of such *in silico* screening and help prioritize targets whose effects remain robust across protocol conditions and parameter variability.

Bibliography

[1] Kilfoil, P.J., Lotteau, S., Zhang, R., Yue, X., Aynaszyan, S., Solymani, R.E., Cingolani, E., Marbán, E., Goldhaber, J.I., 2020. *Distinct features of calcium handling and β-adrenergic sensitivity in heart failure with preserved versus reduced ejection fraction*. Journal of Physiology, 598(22), 5091–5108. doi:10.1113/JP280425.

[2] Durland, L., 2021. *Distinguishing HF with reduced and preserved ejection fraction at the level of individual cardiomyocytes: implications for therapeutic development*. Journal of Physiology, 599(4), 1027–1029. doi:10.1113/JP280739.

[3] Mora, M.T., Zaza, A., Trenor, B., 2023. *Insights from an electro-mechanical heart failure cell model: Role of SERCA enhancement on arrhythmogenesis and myocyte contraction*. Computer Methods and Programs in Biomedicine, 230, 107350. doi:10.1016/j.cmpb.2023.107350.

[4] Zhou, X., Kaur, G., Liu, W., et al., 2024. *Lower diastolic tension may be indicative of higher proarrhythmic propensity in failing human cardiomyocytes*. Scientific Reports, 14, 29184. doi:10.1038/s41598-024-79407-8.

[5] Bartolucci, C., Passini, E., Hyttinen, J., Paci, M., Severi, S., 2020. *Simulation of the Effects of Extracellular Calcium Changes Leads to a Novel Computational Model of Human Ventricular Action Potential With a Revised Calcium Handling*. Frontiers in Physiology, 11, 314. doi:10.3389/fphys.2020.00314.

[6] Bartolucci, C., Forouzandehmehr, M., Severi, S., Paci, M., 2022. *A Novel In Silico Electromechanical Model of Human Ventricular Cardiomyocyte*. Frontiers in Physiology, 13, 906146. doi:10.3389/fphys.2022.906146.

[7] O'Hara, T., Virág, L., Varró, A., Rudy, Y., 2011. *Simulation of the undiseased human cardiac ventricular action potential: model formulation and experimental validation*. PLoS Computational Biology, 7(5), e1002061. doi:10.1371/journal.pcbi.1002061.

[8] Tomek, J., Rodriguez, B., Bub, G., et al., 2019. *Development, calibration, and validation of a novel human ventricular myocyte model in health, disease, and drug block*. eLife, 8, e48890. doi:10.7554/eLife.48890.

[9] Land, S., Park-Holohan, S.-J., Smith, N.P., dos Remedios, C.G., Kentish, J.C., Niederer, S.A., 2017. *A model of cardiac contraction based on novel measurements of tension development in human cardiomyocytes*. Journal of Molecular and Cellular Cardiology, 106, 68–83. doi:10.1016/j.yjmcc.2017.03.008.

[10] Finsberg, H., Wall, S., Chabiniok, R., et al., 2018. *Computational modeling of cardiac electromechanics*. Philosophical Transactions of the Royal Society A, 376(2121), 20170337. doi:10.1098/rsta.2017.0337.

[11] Paci, M., Hyttinen, J., Aalto-Setälä, K., Severi, S., 2013. *Computational Models of Ventricular- and Atrial-Like Human Induced Pluripotent Stem Cell Derived Cardiomyocytes*. Annals of Biomedical Engineering, 41(11), 2334–2348. doi:10.1007/s10439-013-0833-3.

[12] Paci, M., Passini, E., Klimas, A., Severi, S., Hyttinen, J., Rodriguez, B., Entcheva, E., 2020. *All-Optical Electrophysiology Refines Populations of In Silico Human iPSC-CMs for Drug Evaluation*. Biophysical Journal, 118(10), 2596–2611. doi:10.1016/j.bpj.2020.03.018.

[13] Mazhar, F., Regazzoni, F., Bartolucci, C., Corsi, C., Dede', L., Quarteroni, A., Severi, S., 2021. *Electro-Mechanical Coupling in Human Atrial Cardiomyocytes: Model Development and Analysis of Inotropic Interventions*. Computing in Cardiology, 48, 1–4. doi:10.22489/CinC.2021.177.

[14] Mazhar, F., Regazzoni, F., Bartolucci, C., Corsi, C., Dede', L., Quarteroni, A., Severi, S., 2022. *A Novel Human Atrial Electromechanical Cardiomyocyte Model with Mechano-Calcium Feedback Effect*. Computing in Cardiology, 49, 1–4. doi:10.22489/CinC.2022.195.

[15] Mazhar, F., Bartolucci, C., Corsi, C., Severi, S., 2023. *Investigation of Key Cellular Targets in Atrial Fibrillation Induced Electromechanical Remodeling Using Human Atrial Cardiomyocytes Model*. Computing in Cardiology, 50, 1–4. doi:10.22489/CinC.2023.330.

[16] Bartolucci, C., Fabbri, C., Tomasi, C., Sabbatani, P., Severi, S., et al., 2021. *Computational Analysis of Mapping Catheter Geometry for Rotor Detection in Atrial Fibrillation*. Frontiers in Physiology, 12, 732161. doi:10.3389/fphys.2021.732161.

[17] Bartolucci, C., Mazhar, F., Corsi, C., Severi, S., et al., 2024. *Simulation of Cardiac Contractility Modulation with a Human Atrial/Ventricular Electromechanical Cardiomyocyte Model*. Computing in Cardiology, 51, 1–4. doi:10.22489/CinC.2024.405.

[18] Koivumäki, J.T., Seemann, G., Maleckar, M.M., Tavi, P., 2014. *In Silico Screening of the Key Cellular Remodeling Targets in Chronic Atrial Fibrillation*. PLoS Computational Biology, 10(5), e1003620. doi:10.1371/journal.pcbi.1003620.

[19] Muszkiewicz, A., Britton, O.J., Gemmell, P., Passini, E., Sánchez, C., Zhou, X., Carusi, A., Quinn, T.A., Burrage, K., Bueno-Orovio, A., Rodriguez, B., 2016. *Variability in cardiac electrophysiology: Using experimentally-calibrated populations of models to move beyond the single virtual physiological human paradigm*. Progress in Biophysics and Molecular Biology, 120(1–3), 115–127. doi:10.1016/j.pbiomolbio.2015.12.002.

[20] Bers, D.M., 2006. *Altered cardiac myocyte Ca regulation in heart failure*. Physiology (Bethesda), 21, 380–387. doi:10.1152/physiol.00019.2006.

[21] Sutanto, H., Lyon, A., Lumens, J., Schotten, U., Dobrev, D., Heijman, J., 2020. *Cardiomyocyte calcium handling in health and disease: Insights from in vitro and in silico studies*. Progress in Biophysics and Molecular Biology, 157, 54–75. doi:10.1016/j.pbiomolbio.2020.02.002.

[22] Aiba, T., Tomaselli, G.F., 2010. *Electrical remodeling in heart failure*. Journal of Molecular and Cellular Cardiology, 48(6), 911–921. doi:10.1016/j.yjmcc.2010.01.012.

[23] Morotti, S., Grandi, E., 2019. *Quantitative systems models illuminate arrhythmia mechanisms in heart failure: role of the* Na^{+}*–*Ca^{2+}*–CaMKII–ROS feedback*. Wiley Interdisciplinary Reviews: Systems Biology and Medicine, 11, e1434. doi:10.1002/wsbm.1434.

[24] Benitah, J.-P., Perrier, R., Mercadier, J.-J., Pereira, L., Gómez, A.M., 2021. *RyR2 and calcium release in heart failure*. Frontiers in Physiology, 12, 734210. doi:10.3389/fphys.2021.734210.

[25] Dries, E., Santiago, D.J., Gilbert, G., et al., 2018. *Hyperactive ryanodine receptors in human heart failure and ischaemic cardiomyopathy reside outside of couplons*. Cardiovascular Research, 114(11), 1512–1524. doi:10.1093/cvr/cvy088.

[26] Kolstad, T.R., van den Brink, J., Macquaide, N., et al., 2018. *Ryanodine receptor dispersion disrupts* Ca^{2+} *release in failing cardiac myocytes*. eLife, 7, e39427. doi:10.7554/eLife.39427.

[27] Weber, C.R., Piacentino, V., Ginsburg, K.S., Houser, S.R., Bers, D.M., 2003. Na^{+}/Ca^{2+} *exchange current and submembrane* Ca^{2+} *dynamics during the cardiac action potential*. Circulation Research, 92(9), 1029–1037. doi:10.1161/01.RES.0000070120.72657.30.

[28] Kang, T.M., Hilgemann, D.W., 2004. *Multiple transport modes of the cardiac* Na^{+}/Ca^{2+} *exchanger*. Nature, 427(6974), 544–548. doi:10.1038/nature02272.

[29] Antzelevitch, C., Nesterenko, V., Yan, G.X., 2014. *Role of the late sodium current in cardiac electrophysiology and arrhythmogenesis*. Heart Rhythm, 11(10), 1760–1768. doi:10.1016/j.hrthm.2014.06.003.

[30] Roden, D.M., 1998. *Taking the "idio" out of "idiosyncratic": predicting torsades de pointes*. Pacing and Clinical Electrophysiology, 21(5), 1029–1034. doi:10.1111/j.1540-8159.1998.tb00146.x.

[31] Balakina-Vikulova, O.V., Solovyova, O., Panfilov, A.V., Katsnelson, L.B., 2023. *In silico analysis of the contribution of cardiomyocyte–fibroblast electromechanical interaction to the arrhythmia mechanisms under calcium overload*. Frontiers in Physiology, 14, 1123609. doi:10.3389/fphys.2023.1123609.

[32] Standring, S. (Ed.), 2016. *Gray's Anatomy: The Anatomical Basis of Clinical Practice*. 41st ed. Elsevier, New York.

[33] Klabunde, R.E., 2011. *Cardiovascular Physiology Concepts*. 2nd ed. Lippincott Williams & Wilkins, Philadelphia.

[34] Surawicz, B., Knilans, T.K., 2008. *Chou's Electrocardiography in Clinical Practice: Adult and Pediatric*. 6th ed. Saunders/Elsevier.

[35] Shampine, L.F., Reichelt, M.W., 1997. *The MATLAB ODE Suite*. SIAM Journal on Scientific Computing, 18(1), 1–22. doi:10.1137/S1064827594276424.

[36] Shampine, L.F., Reichelt, M.W., Kierzenka, J., 1999. *Solving Index-1 DAEs in MATLAB and Simulink*. SIAM Review, 41(3), 538–552. doi:10.1137/S003614459933425X.

[37] Bartolucci–Passini–Severi Model (BPS2020) MATLAB code, accessed 2026-01-03. Available at: `https://www.mcbeng.it/en/downloads/software/16-bps2020-model.html`.

[38] O'Hara–Rudy Human Ventricular Model (ORd) MATLAB code, accessed 2026-01-03. Available at: `http://rudylab.wustl.edu/research/cell/code/AllCodes.html`.

[39] Piacentino, V., Weber, C.R., Chen, X., Weisser-Thomas, J., Margulies, K.B., Bers, D.M., Houser, S.R., 2003. *Cellular basis of abnormal calcium transients of failing human ventricular myocytes*. Circulation Research, 92, 651–658. https://doi.org/10.1161/01.RES.0000062469.83985.9B.

[40] Pieske, B., Sütterlin, M., Schmidt-Schweda, S., Minami, K., Meyer, M., Olschewski, M., Holubarsch, C., Just, H., Hasenfuss, G., 1996. *Diminished post-rest potentiation of contractile force in human dilated cardiomyopathy: Functional evidence for alterations in intracellular* Ca^{2+} *handling*. Journal of Clinical Investigation, 98, 764–776. https://doi.org/10.1172/JCI118849.

[41] Mulieri, L.A., Hasenfuss, G., Leavitt, B., Allen, P.D., Alpert, N.R., 1992. *Altered myocardial force-frequency relation in human heart failure*. Circulation, 85, 1743–1750. https://doi.org/10.1161/01.CIR.85.5.1743.

[42] Hasenfuss, G.P., Mulieri, L.A., Leavitt, B.J., Allen, P.D., Haeberle, J.R., Alpert, N.R., 1992. *Alteration of contractile function and excitation-contraction coupling in dilated cardiomyopathy*. Circulation Research, 70, 1225–1232. https://doi.org/10.1161/01.RES.70.6.1225.

[43] Mashali, M.A., Saad, N.S., Canan, B.D., Elnakish, M.T., Milani-Nejad, N., Chung, J.H., Schultz, E.J., Kiduko, S.A., Huang, A.W., Hare, A.N., Peczkowski, K.K., Fazlollahi, F., Martin, B.L., Murray, J.D., Campbell, C.M., Kilic, A., Whitson, B.A., Mokadam, N.A., Mohler, P.J., Janssen, P.M.L., 2021. *Impact of etiology on force and kinetics of left ventricular end-stage failing human myocardium*. Journal of Molecular and Cellular Cardiology, 156, 7–19. https://doi.org/10.1016/J.YJMCC.2021.03.007.

[44] Drouin, E., Lande, G., Charpentier, F., 1998. *Amiodarone reduces transmural heterogeneity of repolarization in the human heart*. Journal of the American College of Cardiology, 32, 1063–1067. https://doi.org/10.1016/S0735-1097(98)00330-1.

[45] Li, G.-R., Lau, C.-P., Leung, T.-K., Nattel, S., 2004. *Ionic current abnormalities associated with prolonged action potentials in cardiomy-*

ocytes from diseased human right ventricles. Heart Rhythm, 1, 460–468. https://doi.org/10.1016/j.hrthm.2004.06.003.

[46] Lindner, M., Erdmann, E., Beuckelmann, D.J., 1998. *Calcium content of the sarcoplasmic reticulum in isolated ventricular myocytes from patients with terminal heart failure*. Journal of Molecular and Cellular Cardiology, 30, 743–749. https://doi.org/10.1006/jmcc.1997.0626.

[47] Holubarsch, C., Lüdemann, J., Wiessner, S., Ruf, T., Schulte-Baukloh, H., Schmidt-Schweda, S., Pieske, B., Posival, H., Just, H., 1998. *Shortening versus isometric contractions in isolated human failing and non-failing left ventricular myocardium: Dependency of external work and force on muscle length, heart rate and inotropic stimulation*. Cardiovascular Research, 37, 46–57. doi:10.1016/S0008-6363(97)00215-0.

[48] Margara, F., Wang, Z.J., Levrero-Florencio, F., Santiago, A., Vázquez, M., Bueno-Orovio, A., Rodriguez, B., 2021. *In-silico human electro-mechanical ventricular modelling and simulation for drug-induced pro-arrhythmia and inotropic risk assessment*. Progress in Biophysics and Molecular Biology, 159, 58–74. doi:10.1016/j.pbiomolbio.2020.06.007.